Does ring current heating generate the observed O$ˆ+$ shell?

Jonathan Krall[1], J.D. Huba[2], and Mei-Ching H. Fok[3]

[1]Naval Research Laboratory
[2]Syntek Technologies
[3]NASA Goddard Space Flight Center

November 26, 2022

Abstract

The Naval Research Laboratory (NRL) Sami3 is Also a Model of the Ionosphere (SAMI3) ionosphere/plasmasphere code is used to examine the effect of ring current heating during a storm. With a ring current heating function added to SAMI3, a cold thermal (< 1 eV) oxygen ion outflow is produced, with O$ˆ+$ density and location similar to observations of the so-called "oxygen torus.' The ring current heating function is based on a Comprehensive Inner Magnetosphere-Ionosphere (CIMI) model simulation of the 2015 October 7 storm. We find that the ring current can heat plasmasphere electrons, subsequently heating plasmasphere H$ˆ+$, and ionosphere O$ˆ+$. The resulting O$ˆ+$ outflows resemble observed O$ˆ+$ enhancements in the inner magnetosphere.

Does ring current heating generate the observed O^+ shell?

J. Krall[1], J. D. Huba[2], and M.-C. Fok[3]

[1]Plasma Physics Division, Naval Research Laboratory, Washington, District of Columbia, USA
[2]Syntek Technologies, Fairfax, VA, USA
[3]NASA Goddard Space Flight Center, Greenbelt, Maryland, USA.

Key Points:

- Simulated ring current heating produces an outflow of "cold" (< 1 eV) oxygen ions into the magnetosphere
- Model oxygen ion densities and positions are similar to observations of the so-called "oxygen torus"
- Model oxygen ion enhancements resemble a partial toroidal shell that extends outwards along the geomagnetic field

Corresponding author: Jonathan Krall, `jonathan.krall@nrl.navy.mil`

Abstract

The Naval Research Laboratory (NRL) Sami3 is Also a Model of the Ionosphere (SAMI3) ionosphere/plasmasphere code is used to examine the effect of ring current heating during a storm. With a ring current heating function added to SAMI3, a cold thermal ($<$ 1 eV) oxygen ion outflow is produced, with O^+ density and location similar to observations of the so-called "oxygen torus." The ring current heating function is based on a Comprehensive Inner Magnetosphere-Ionosphere (CIMI) model simulation of the 2015 October 7 storm. We find that the ring current can heat plasmasphere electrons, subsequently heating plasmasphere H^+, and ionosphere O^+. The resulting O^+ outflows resemble observed O^+ enhancements in the inner magnetosphere.

Plain Language Summary

The near-Earth environment includes relatively low-energy "cold" ions with temperatures less than 10^5 K (8.6 eV) and much higher energy ions. We specifically consider the cold plasmasphere, the magnetically-contained extension of the ionosphere into space, and the ring current, a high energy (1-100 keV) population of O^+ and H^+ ions generated during a geomagnetic storm. We numerically model the interaction between these populations in search of an explanation for the cold oxygen ions that are observed near the edge of the plasmasphere. Results suggest that the ring current heats plasmasphere electrons, plasmasphere H^+, and ionosphere O^+. The heated O^+ flows upward along the geomagnetic field, forming the "oxygen torus" that has been observed by numerous spacecraft.

1 Introduction

Cold, dense ion populations in the inner magnetosphere play a significant role in space weather through their effect on electromagnetic waves (Millan & Thorne, 2007; Bortnik & Thorne, 2007) that generate energetic ions in the Van Allen radiation belts. The so-called oxygen torus (hereafter the O^+ enhancement or O^+ shell), an enhancement of O^+ ions "in the outer plasmasphere" (Chappell, 1982), appears to be a dominant contributor to the stormtime cold ion mass outside of the plasmapause.

This O^+ enhancement was first identified (Chappell, 1982) using the Retarding Ion Mass Spectrometer (RIMS) instrument (Chappell et al., 1981) on the Dynamics Explorer (DE) spacecraft and has been observed many times since. Roberts et al. (1987) analyzed DE:RIMS data from 1981 through 1984, finding heavy ion enhancements at all local times. Using ground-based magnetometer field-line resonance measurements of mass density from the SAMNET and IMAGE arrays in the UK and Scandinavia, in conjunction with IMAGE spacecraft (Burch, 2000) electron and He^+ densities, Grew et al. (2007) found enhanced O^+ densities near local midnight, about 12 hours after storm onset for a strong (Dst < -150 nT) storm. Using the Van Allen Probes (Reeves, 2007), Nosé et al. (2015) found an enhancement in average ion mass in the dawn sector for $3 \leq L \leq 4.5$, where L is the McIlwain parameter (McIlwain, 1961). Analyzing data from the Arase satellite (Miyoshi et al., 2018) and Van Allen Probe A spacecraft at approximately the same universal time, Nosé et al. (2018) found a density enhancement at 5 h MLT, but not 13–14 h MLT, suggesting a crescent shape instead of a torus.

In this letter, we describe initial modeling that tests the hypothesis that this "cold" O^+ population represents an outflow of heated O^+ ions from the topside ionosphere with the ring current being a viable heat source. By "cold," we mean a thermal (Maxwellian) particle population with a temperature below the typical threshhold (a few eV, in the plasmasphere) for direct detection due to spacecraft charging (Grard et al., 1983). Storm-generated ring current ions have energies in the 1–100 keV range (Daglis et al., 1999). Ring current ions, which hold the bulk of the ring current energy, interact with magne-

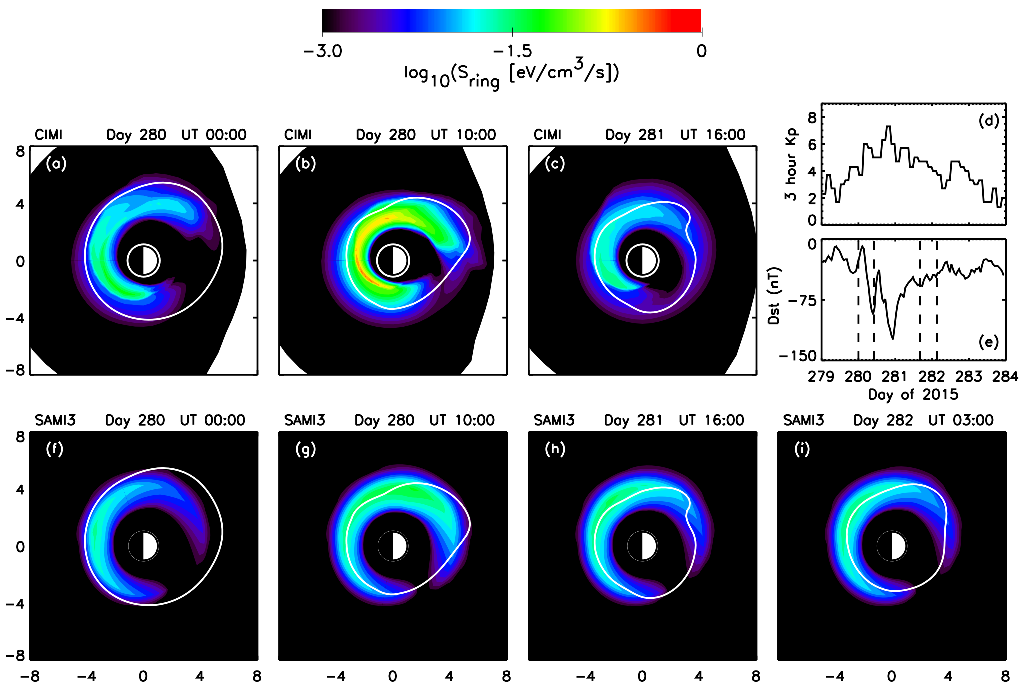

Figure 1. (a–c) CIMI model output showing the log of the heat transferred to the electrons at selected times plotted as color contours in the magnetic equatorial plane. (d) Kp and (e) Dst geomagnetic indices which peaked on day 280 (7 October) of 2015. (f–i) SAMI3 ring current heating function. A single contour line in panels a–c and f–i indicates SAMI3 plasmasphere electron density $n_e = 100$ cm^{-3}. Each column corresponds to a UT value marked by a vertical dashed line in panel (e). SAMI3 and CIMI numerical outputs for this and other figures are included in supplemental material for this publication.

tosphere neutral populations through charge exchange (Ilie et al., 2013), creating the energetic neutral atoms that allow the ring current to be imaged (Roelof, 1987). Ring current ions also heat the background plasma through Coulomb collisions (Fok et al., 1995) with the dominant effect being electron heating. In fact, when Chappell (1982) identified the O^+ enhancement in DE:RIMS data, he suggested ring current heating as a possible mechanism: "This torus may be explained by an enhanced thermal diffusion in the outer plasmasphere due to a heating of the outer plasmasphere by the hot magnetospheric plasma." The specific hypothesis of ring current heating was examined by Horwitz et al. (1986) and by Roberts et al. (1987, Fig. 17). While these early studies suggest both Coulomb collisions and wave-particle interactions as candidate heating mechanisms, we consider only Coulomb collisions in the present study.

The present study is new in the sense that we simulate the effect of a specific source for the O^+ shell: the impact of ring current heating on plasmasphere electrons and ionosphere O^+, with both processes, the ring current and the ion outflow, being simulated by solving the underlying first-principles equations. In prior modeling of this O^+ ion population, such as Nosé et al. (2015), O^+ ions are placed in the inner magnetosphere as an initial condition.

As an example, we consider a specific event, the 2015 October 7 (day 280) storm. We use the Comprehensive Inner Magnetosphere-Ionosphere (CIMI) model (Fok et al., 2014) to model this event and compute ring current heating. Based on CIMI calculations of electron heating, we construct a model heating function for use in the SAMI3 (Sami3 is Also a Model of the Ionosphere) ionosphere/plasmasphere model (Huba & Krall, 2013). The present study is speculative in the sense that the heating is through the specification of a heating function that depends only on the Dst index. A more careful exploration of this subject will require ionosphere/plasmasphere and ring current models that are self-consistently coupled (e.g. Huba et al., 2017).

2 CIMI modeling of ring current heating

We use CIMI to simulate days 279 through 281 of 2015. The CIMI model (Fok et al., 2014) self-consistently solves the bounce-averaged Boltzmann convection-diffusion equation for ring current particles O^+ and H^+. CIMI is based on the earlier Comprehensive Ring Current Model, which compares well to geomagnetic index and imaging observations (Buzulukova et al., 2010). CIMI computes the energy lost from the ring current via Coulomb collisions with background electrons and ions. The modeling of the background plasmasphere in CIMI is based on the dynamic global core plasmasphere model (DGCPM) (Ober et al., 1997). Because energy losses are dominated by electron Coulomb collisions (Fok et al., 1995), we focus on this dominant mechanism. Figure 1(a–c) shows the CIMI-computed rate at which plasmasphere electrons are heated by ring current ions via Coulomb collisions, plotted in the magnetic equatorial plane.

Because CIMI is not coupled to the SAMI3 ionosphere/plasmasphere model (described below), we used the CIMI model output at a 1 hour cadence for this and one other mild storm (2013 March 17) as the basis for constructing a heating function for use in SAMI3. The electron heating function, plotted in Figure 1(f–i), is a function only of the Dst index, shown in Figure 1(e) for this storm.

The peak heating rate $S_{RC,peak}[\text{eV-cm}^{-3}\text{s}^{-1}] = (-\text{Dst[nT]})^{1/2}/200$ for Dst<0. In MLT, the peak heating position decreases linearly from 2.0 h MLT for Dst $=0$ to 11.5 h MLT for Dst ≤ -145 nT. The heating function versus MLT falls to a non-zero minimum at 8 h MLT. At fixed MLT, peak heating is at $L = 3.5{+}\Delta L$, where ΔL, introduced to account for the outward bulge in the heating region in the afternoon sector, increases linearly from 0 at 24 h MLT to 1 at the position of the bulge in MLT, t_{bulge}. At MLT positions dawnward of t_{bulge}, ΔL decreases linearly from 1 at t_{bulge} to about 0.5 at 8 h MLT. The bulge position t_{bulge} decreases linearly from 18 h MLT for Dst $\geq$ 0 to 12.0 h MLT for Dst ≤ -150 nT. Heating is applied uniformly along each field line, but only for geocentric radius $r > 2.7R_E$; it is introduced as an additional term in the SAMI3 electron energy equation (Huba et al., 2000, Eq. 31). Both the CIMI model output and the SAMI3 heating subroutine are available in the data archive.

This heating function captures the basic properties of the CIMI output for the two events simulated. Specifically, as the storm strengthens (Figure 1a,b), the peak heating shifts towards lower MLT, the heating region in the afternoon sector bulges out away from Earth, and the position of the maximum outward shift of the bulge moves towards lower MLT. In addition to computing heating at the equator, Figure 1(a–c), CIMI computed field-line integrated heating (not shown). In order to approximate the CIMI equatorial and integrated Coulomb heating results, the heating function is nonzero only above altitude 1.7 R_E ($r > 2.7R_E$). While some features of the computed heating, Figure 1(a–c), are not present in the corresponding plots of the model heating function, Figure 1(f–h), the bulk properties are similar enough to provide a test of the heating effect.

3 SAMI3 modeling of the O^+ shell

To simulate this event, we use the SAMI3 ionosphere/plasmasphere model (Huba & Krall, 2013) with appropriate inputs, such as daily values for $F_{10.7}$ ($\simeq 81$), $F_{10.7A}$ ($\simeq$ 110), and the Ap index. For this case we used a Kp-driven VSMC (Volland-Stern- Man-

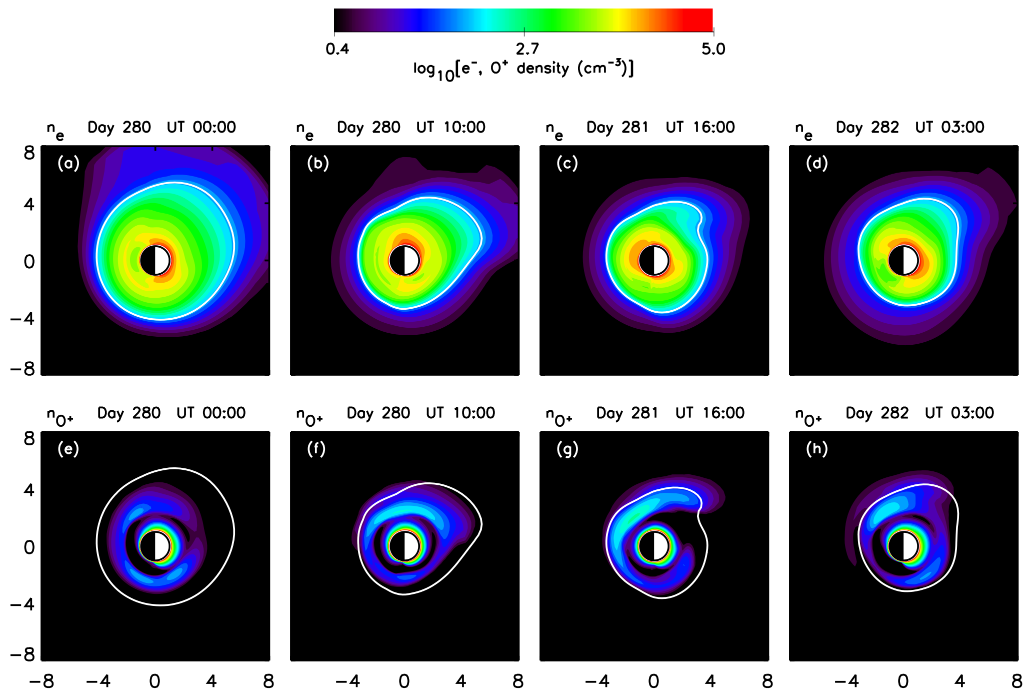

Figure 2. SAMI3 output showing (a–d) $\log_{10} n_e$ and (e–h) $\log_{10} n_{O+}$. Each column is at the same time as the corresponding column in Figure 1.

yard/Chen Volland, 1973; Stern, 1975; Maynard & Chen, 1975; Reinisch et al., 2009) function for the magnetospheric convection potential; Kp versus time is shown in Figure 1(d) for this event. We performed additional runs using the empirical Weimer05 (Weimer, 2005) model in place of the VSMC function and found that the results were not sensitive to details of the high-latitude convection potential.

SAMI3 includes 7 ion species (H^+, He^+, O^+, N^+, NO^+, N_2^+, O_2^+) with an energy equation being solved for H^+, He^+, O^+ and the electrons. Each species is represented by a fluid that flows dynamically along the magnetic field (Huba et al., 2000). To avoid erroneously high fluid velocities at high altitudes (Huba & Joyce, 2013, see Fig. 3), the inertial term is retained in the field-aligned dynamical equations. Plasma motions across field lines are approximated to be $\mathbf{E}\times\mathbf{B}$ drifts. Based on SAMI2 and SAMI3 test runs of this and one other event (the 2013 March 17 storm) we used a grid of 124 “field lines”, 96 longitudes, and 404 points long each field line. The large number of points along each field line is necessary to capture plasma and heat flows.

Figure 2 shows the dynamics of the plasmasphere and the O^+ enhancement, plotted in the magnetic equatorial plane. We see the usual features of the plasmasphere during a storm, such as the sunward extension of the plasmasphere when the storm is strongest, Figure 2(b), and the duskward rotation and sharpening of the plume as the storm weakens, Figure 2(c).

Consistent with Nosé et al. (2018), we do not always find a complete torus shape in the equatorial plane. Similar to Figure 2(e,g,h), where the O^+ density is very low in the hours immediately following noon, Nosé et al. (2018) found a weak ($M = 3.5$ amu) O^+ enhancement at 05:00 MLT but not in the early afternoon sector(13-14:00 MLT). The circumstance of the Nosé et al. (2018) measurements, two days into an extended period of Dst $\simeq -50$ nT, is similar to that of Figure 2(h), over one day past the peak of

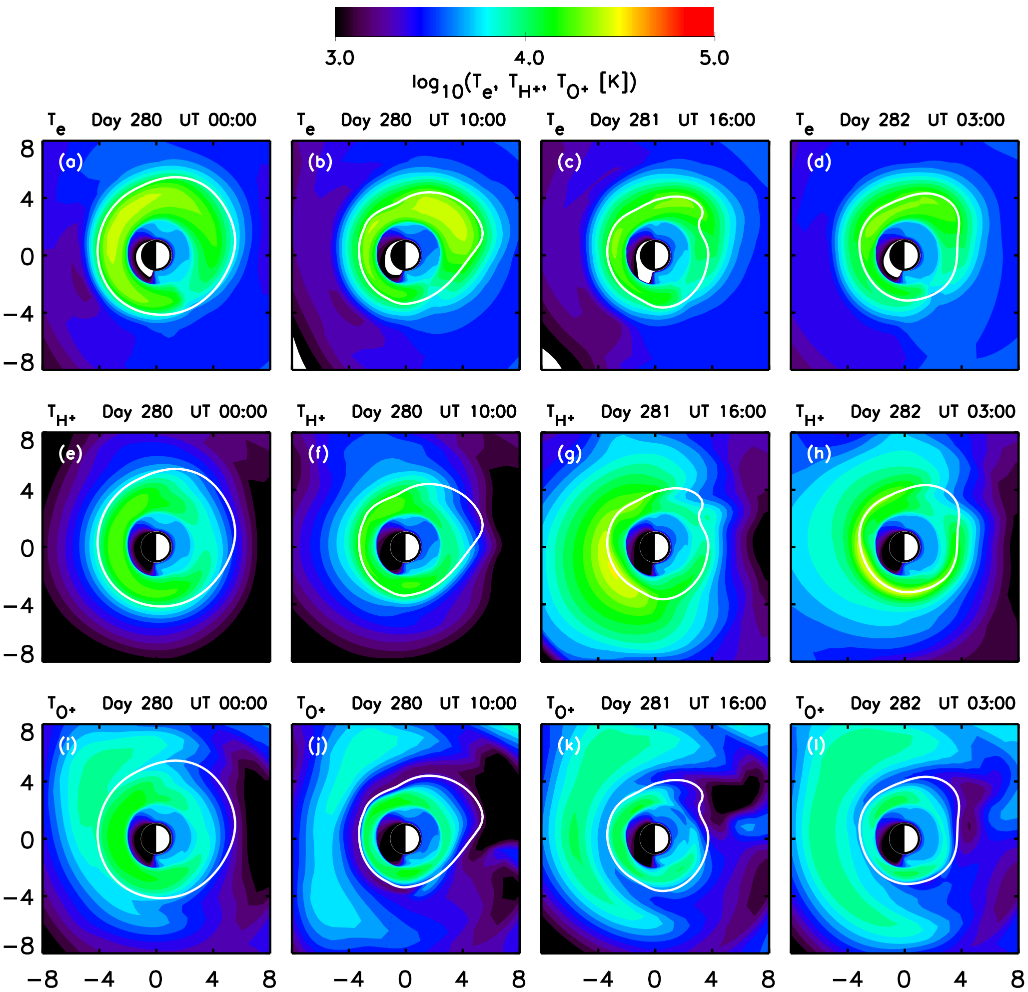

Figure 3. SAMI3 model output showing (a–d) the log of the electron temperature T_e, (e–h) the log of the H^+ temperature, and (i–l) the log of the O^+ temperature. Each column is at the same time as the corresponding column in Figures 1 and 2.

the storm with Dst $\simeq -50$ nT. When the storm is strongest, however, Figure 2(f), the O^+ enhancement more completely surrounds Earth.

Away from the peak of the storm, Figure 2(e,g,h), SAMI3 shows local peaks in the O^+ density after dusk and after dawn. These O^+ enhancements are consistent with Roberts et al. (1987), who show examples of "heavy ion enhancements" at 2100 MLT (Roberts et al., 1987, Figs. 1 and 5), 2000 MLT (Roberts et al., 1987, Fig. 3), and 0800 MLT (Roberts et al., 1987, Fig. 4). Roberts et al. (1987, Fig. 8a) also show that O^+ enhancements occur most often in the pre-midnight and post-dawn hours. Consistent with our results and with the Nosé et al. (2018) suggestion of a crescent instead of a torus, Roberts et al. (1987, Fig. 7a), suggest that the O^+ enhancement is weakest between 1100 and 1400 MLT.

Figure 3 shows the electron, H^+, and O^+ temperatures. The results are suggestive. For example, T_e is largest before and during the peak of the storm, Figure 3(a,b), while T_{H^+} is largest after the peak of the storm Figure 3(g,h). This suggests a time scale on the order of 1 day for heat transfer from electrons to H^+ ions. Similar to our result, a

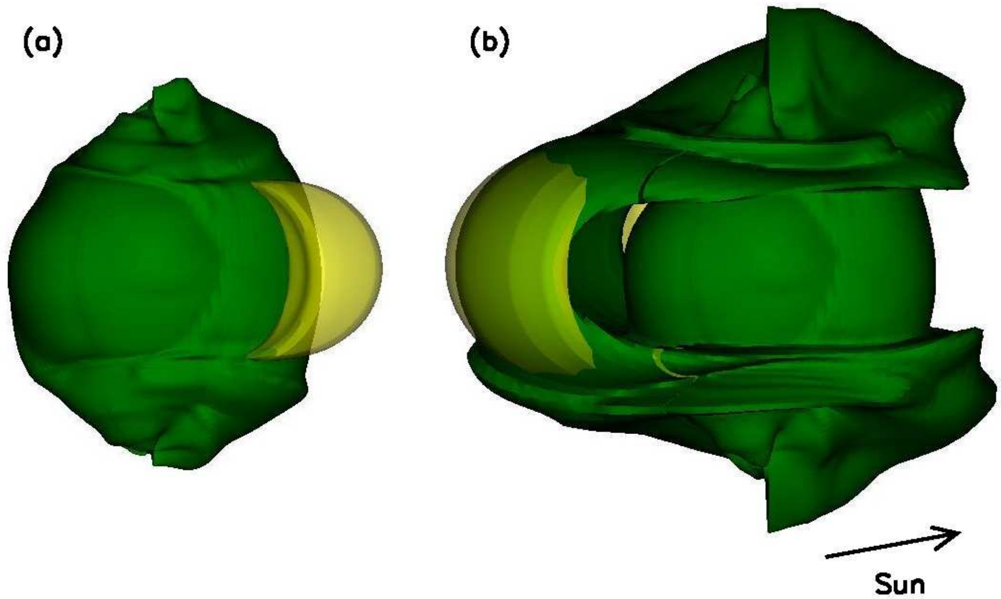

Figure 4. SAMI3 result for Day 281, 0600UT, showing isosurfaces where O^+ density is at 100 cm^{-3} (green) for (a) the case with no heating and (b) with heating. The yellow isosurface indicates an electron temperature of 5.5×10^3 K (panel a) and 2.0×10^4 K (panel b). An arrow indicates the direction to the Sun.

jump in H^+ temperature from about 6×10^3 to about 3×10^4 at the plasmapause is seen by Comfort et al. (1988) in DE:RIMS data. In our case, however, the region of elevated T_{H^+} straddles the plasmapause. Similar to Horwitz et al. (1986), model T_e and T_{H^+} (but not T_{O^+}) enhancements are "sometimes strikingly well correlated." In our case, correlation of T_{H^+} with T_e appears strongest early in the storm. Throughout the storm, the pattern of elevated T_e closely matches the heating (compare Figure 3a–d to Figure 1f–i), while the T_{H^+} morphology suggests that H^+ is affected by corotation of the plasmasphere. While the minimum in the heating fuction is a 8 h MLT, the corresponding mimimum in T_{H^+} has rotated around to the afternoon sector. The morphology of the O^+ density Figure 2(e–h) is also suggestive of corotation, an effect also seen in the modeling of Nosé et al. (2015).

The T_{O^+} plots, Figure 3(i–l), show a heated O^+ population, corresponding to the O^+ shell of Figure 2(e–h), that remains "cold," with $T_{\mathrm{O}^+} < 1$ eV. We suggest that T_{O^+} in the O^+ shell is less than T_{H^+} and T_e because heated O^+ in the ionosphere flows outward on flux tubes that expand with height, cooling adiabatically as it expands. A low density heated O^+ population is evident on the night side at $L > 4$; its significance is not clear at this time.

Figure 4 shows the effect of the heating on the O^+ density in the plasmasphere. A yellow isosurface in Figure 4(b) ($T_e = 2.0 \times 10^4$ K) indicates the direct effect of the heating. The shape of the green isosurface ($n_{\mathrm{O}^+} = 100$ cm^{-3}) in Figure 4(b) indicates O^+ outflow along field lines. In the peak heating region, the O^+ 100 cm^{-3} isosurface reaches the equator, forming a high density shell of O^+. When the same simulation is run without ring current heating, Figure 4(a), the O^+ shell is absent and the hottest electron temperatures ($T_e = 5.5 \times 10^3$ K) are on the dayside. However, O^+ upwellings at higher latitudes are present in both Figures 4(a) and (b).

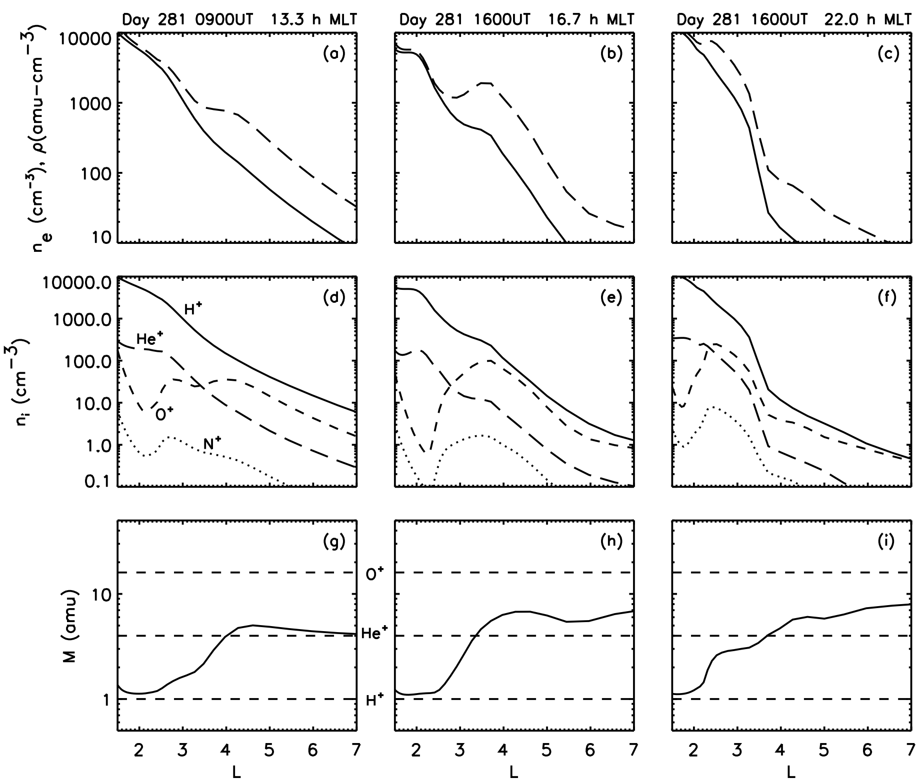

Figure 5. Radial profiles in the magnetic equatorial plane showing (a–c) electron number density n_e (solid line) and ion mass density ρ (dashed line), (d–f) number density for H^+, He^+, N^+ and O^+ and (g–i) average mass density M (horizontal dashed lines indicate the H^+, He^+, and O^+ masses). Plots in the second an third columns correspond to Figure 2(c,g).

4 Further comparison to observations

Figure 5 shows radial profiles of n_e (cm^{-3}) and ρ (amu-cm^{-3}) along with corresponding profiles showing composition and average mass density M. In Figure 5, each column corresponds to a fixed UT and MLT. In all three cases we find both the O$^+$ shell and a corresponding N$^+$ shell at much lower density ($n_{\mathrm{O}^+}/n_{\mathrm{N}^+} > 10$). In each composition plot, Figure 5(d–f), we find an O$^+$ profile that falls for $L < 2$, reaches a minimum, and rises thereafter. It is the O$^+$ density enhancement outside of the O$^+$ minumim that we call the O$^+$ enhancement or O$^+$ shell.

Figure 5(a,b) compares well to Takahashi et al. (2008, Fig. 6), who showed electron and mass densities derived from CRRES (Combined Release and Radiation Effects Satellite) (Johnson & Kierein, 1992) observations of the 1991 August 27 storm. Assuming that the plasma inside the the plasmapause is primarily H$^+$, they found that mass densities inside and outside of the plasmapause were consistent with a gradual decrease in ρ with L across the plasmapause. This implies the jump in the average ion mass at the plasmapause that we see in Figure 5(g,h). Because these CRRES observations of ρ, M, are limited to $L > 4$, the dip in ρ at the plasmapause that is evident in Figure 5(a,b) is not seen in the Takahashi et al. (2008, Fig. 6) observation. However, the dip in ρ at the plasmapause is similar to that seen by Fraser et al. (2005, Fig. 1b), in evening sector, 19.4–19.8 h MLT. These profiles, in both Figure 5(a,b) and Takahashi et al. (2008, Fig. 6), are shown for the afternoon sector, at or near the magnetic equator, a few hours after the peak of the storm.

The profiles of Figure 5(d–f) are similar to Roberts et al. (1987, Fig. 5), who also find an N$^+$ enhancement coincident with the O$^+$ enhancement. In Roberts et al. (1987), the N$^+$ density is about 1/10 of the O$^+$ density. In their case, ion composition was measured at approximately 20 h MLT and after three days of Dst $\simeq -30$ nT. In our case we find similar profiles 18 hours after the peak of the storm, but at 15.2 h MLT, Figure 5(e). At 22 h MLT, Figure 5(f), we find the O$^+$ shell inside the plasmapause, again coincident with a low-density N$^+$ shell. The M versus L profile of Figure 5(i) shows the usual jump in the average density at the plasmapause, but it is a smaller jump than is seem in Figure 5(g,h). Figure 5(i) shows an enhancement in M inside the plasmapause coincident with the O$^+$ shell. This is similar to that seen in Nosé et al. (2015, Fig. 6 A-4).

5 Discussion

While these results are far from definitive, they suggest that the ring current heating hypothesis is a good candidate explanation for the O$^+$ shell. Horwitz et al. (1986) and Liemohn et al. (2000) suggest that the ring current heating effect will be most intense where the ring current overlaps the plasmasphere. While this is not contradicted by our present results, we find that the strength and location of the heating-generated O$^+$ population is not sensitive to the shape of the plasmasphere. Specifically, when we repeated our simulations using the empirical Weimer05 magnetosphere potential model in place of the VSMC model, we find similar results. Interchange modes (Pierrard & Lemaire, 2004), which can also affect the overlap between the plasmapause and the heating region, are not presently included in the SAMI3 model.

In Figures 1–3 we approximate the plasmapause with a contour at 100 cm^{-3}. In Figure 5(e), however, the location of the plasmapause is ambiguous, a situation also evident in Horwitz et al. (1986, Fig. 3e and 7d). As noted by Roberts et al. (1987), the O$^+$ enhancement "is almost always observed in the region of the plasmasphere just inside the plasmapause and has been seen at all local times." These results confirm that the O$^+$ shell is often inside the plasmapause, Figure 5(f), or straddling the plasmapause, Figure 5(d). An observation where the O$^+$ shell straddles the plasmapause is provided by Fraser et al. (2005, Fig. 1a). In fact, further examinaton of Nosé et al. (2015, Fig. 6) reveals the enhancement of M inside the plasmapause to be a common feature. While measurements of O^+ enhancements within the plasmapause have not been emphasized in the recent literature, they have been reported.

Finally, we note that stormtime temperature and density effects are also observable in the ionosphere. Because this modeling effort does not include penetration electric fields, we do not reproduce storm-enhanced densities. We do, however, find stormtime ionosphere electron temperature increases of about 1000 K, similar to those measured at, for example, Millstone Hill (42.6°N, 71.5°W) (e.g. Pavlov & Buonsanto, 1997; Liu et al., 2016).

6 Conclusion

In this study, we have used a CIMI ring current heating calculation to guide a SAMI3 ionosphere/plasmasphere simuation of the effect of ring current heating during a storm. With a model ring current heating function added to the SAMI3 model, a cold (< 1 eV), thermal oxygen ion outflow was produced. While the resulting model O^+ density resembles an L-shell rather than a torus, its location, density, composition and temperature are similar to observations of the so-called oxygen torus.

Our results suggest that the ring current can heat plasmasphere electrons, plasmasphere H^+, and ionosphere O^+ and that resulting O^+ outflows can account for observed O^+ enhancements. However, these results demonstrate only the viability of the mechanism. Coupled SAMI3/CIMI simulations of specific events, with robust comparisons to data, will be needed to resolve this question. In further simulations, the SAMI3 and CIMI codes will need to be self-consitently coupled both electrodynamically (e.g. Huba et al., 2017) and thermodynamically. We intend to perform such modeling in the near future.

Acknowledgments

This research was supported by NRL Base Funds, NASA Grand Challenge award NNH17AE97I, and NASA Living With a Star award 80NSSC19K0089. The authors thank Drs. Peter Chi (UCLA) and Jerry Goldstein (SRI) for helpful discussions. Numerical information associated with each of the CIMI and SAMI3 figures are available from the publisher as supporting information for this publication. In addition, the numerical information associated with each CIMI and SAMI3 figure, the CIMI numerical heating output file, and the SAMI3 heating-function FORTRAN code, are available at https://doi.org/10.5281/zenodo.3834161.

References

Bortnik, J., & Thorne, R. M. (2007). The dual role of ELF/VLF chorus waves in the acceleration and precipitation of radiation belt electrons. *Journal of Atmospheric and Solar-Terrestrial Physics*, *69*(3), 378–386. doi: 10.1016/j.jastp.2006.05.030

Burch, J. L. (2000). Image mission overview. *Space Sci. Rev.*, *91*, 1–14. doi: 10.1023/A:1005245323115

Buzulukova, N., Fok, M.-C., Goldstein, J., Valek, P., McComas, D. J., & Brandt, P. C. (2010). Ring current dynamics in moderate and strong storms: Comparative analysis of TWINS and IMAGE/HENA data with the Comprehensive Ring Current Model. *Journal of Geophysical Research: Space Physics*, *115*(A12). doi: 10.1029/2010JA015292

Chappell, C. R. (1982). Initial observations of thermal plasma composition and energetics from Dynamics Explorer-1. *Geophysical Research Letters*, *9*(9), 929–932. doi: 10.1029/GL009i009p00929

Chappell, C. R., Fields, S. A., Baugher, C. R., Hoffman, R. A., Hanson, W. B., Wright, W. W., … Nagy, A. F. (1981). The retarding ion mass spectrometer on Dynamics Explorer-A. *Space Science Instrumentation*, *5*(4), 477–491.

Comfort, R. H., Newberry, I. T., & Chappell, C. R. (1988). Preliminary statistical survey of plasmaspheric ion properties from observations by DE 1/RIMS. In *Modeling magnetospheric plasma* (pp. 107–114). American Geophysical Union (AGU). doi: 10.1029/GM044p0107

Daglis, I. A., Thorne, R. M., Baumjohann, W., & Orsini, S. (1999). The terrestrial ring current: Origin, formation, and decay. *Reviews of Geophysics*, *37*(4), 407–438. Retrieved from `http://dx.doi.org/10.1029/1999RG900009` doi: 10.1029/1999RG900009

Fok, M.-C., Buzulukova, N. Y., Chen, S.-H., Glocer, A., Nagai, T., Valek, P., & Perez, J. D. (2014). The Comprehensive Inner Magnetosphere-Ionosphere model. *Journal of Geophysical Research: Space Physics*, *119*(9), 7522–7540. doi: 10.1002/2014JA020239

Fok, M.-C., Craven, P. D., Moore, T. E., & Richards, P. G. (1995). Ring current-plasmasphere coupling through coulomb collisions. In *Cross-scale coupling in space plasmas* (pp. 161–171). American Geophysical Union (AGU). doi: 10.1029/GM093p0161

Fraser, B. J., Horwitz, J. L., Slavin, J. A., Dent, Z. C., & Mann, I. R. (2005). Heavy ion mass loading of the geomagnetic field near the plasmapause and ULF wave implications. *Geophysical Research Letters*, *32*(4). doi: 10.1029/2004GL021315

Grard, R., Knott, K., & Pedersen. (1983). Spacecraft charging effects. *Space Science Reviews*, *34*(3), 289–304. doi: 10.1007/BF00175284

Grew, R. S., Menk, F. W., Clilverd, M. A., & Sandel, B. R. (2007). Mass and electron densities in the inner magnetosphere during a prolonged disturbed interval. *Geophysical Research Letters*, *34*(2). doi: 10.1029/2006GL028254

Horwitz, J. L., Brace, L. H., Comfort, R. H., & Chappell, C. R. (1986). Dual-spacecraft measurements of plasmasphere-ionosphere coupling. *Journal of Geophysical Research: Space Physics*, *91*(A10), 11203-11216. doi: 10.1029/JA091iA10p11203

Huba, J. D., & Joyce, G. (2013). Numerical methods in modeling the ionosphere. In J. D. Huba, R. W. Schunk, & G. V. Khazanov (Eds.), *Modeling the ionosphere thermosphere system* (Vol. 201, pp. 49–55). Washington, DC: American Geophysical Union.

Huba, J. D., Joyce, G., & Fedder, J. A. (2000). SAMI2 (Sami2 is another model of the ionosphere): A new low-latitude ionosphere model. *Journal of Geophysical Research*, *105*(A10), 23035–23053. doi: 10.1029/2000JA000035

Huba, J. D., & Krall, J. (2013). Modeling the plasmasphere with SAMI3. *Geophysical Research Letters*, *40*, 6–10. doi: 10.1029/2012GL054300

Huba, J. D., Sazykin, S., & Coster, A. (2017). SAMI3-RCM simulation of the 17 March 2015 geomagnetic storm. *Journal of Geophysical Research: Space Physics*, *122*(1), 1246–1257. (2016JA023341) doi: 10.1002/2016JA023341

Ilie, R., Skoug, R. M., Funsten, H. O., Liemohn, M. W., Bailey, J. J., & Gruntman, M. (2013). The impact of geocoronal density on ring current development. *Journal of Atmospheric and Solar-Terrestrial Physics*, *99*, 92–103. doi: 10.1016/j.jastp.2012.03.010

Johnson, M. H., & Kierein, J. (1992). Combined release and radiation effects satellite (CRRES): Spacecraft and mission. *Journal of Spacecraft and Rockets*, *29*(4), 556-563. doi: 10.2514/3.55641

Liemohn, M. W., Kozyra, J. U., Richards, P. G., Khazanov, G. V., Buonsanto, M. J., & Jordanova, V. K. (2000). Ring current heating of the thermal electrons at solar maximum. *Journal of Geophysical Research: Space Physics*, *105*(A12), 27767–27776. doi: 10.1029/2000JA000088

Liu, J., Wang, W., Burns, A., Yue, X., Zhang, S., Zhang, Y., & Huang, C. (2016). Profiles of ionospheric storm-enhanced density during the 17 March 2015 great storm. *Journal of Geophysical Research: Space Physics*, *121*(1), 727–744. doi: 10.1002/2015JA021832

Maynard, N. C., & Chen, A. J. (1975). Isolated cold plasma regions: Observations and their relation to possible production mechanisms. *Journal of Geophysical Research*, *80*(7), 1009–1013. doi: 10.1029/JA080i007p01009

McIlwain, C. E. (1961). Coordinates for mapping the distribution of magnetically trapped particles. *Journal of Geophysical Research*, *66*(11), 3681–3691. doi: 10.1029/JZ066i011p03681

Millan, R. M., & Thorne, R. M. (2007). Review of radiation belt relativistic electron losses. *Journal of Atmospheric and Solar-Terrestrial Physics*, *69*(3), 362–377. doi: 10.1016/j.jastp.2006.06.019

Miyoshi, Y., Shinohara, I., Takashima, T., Asamura, K., Higashio, N., Mitani, T., ... Seki, K. (2018). Geospace exploration project ERG. *Earth, Planets and Space*, *70*(1), 101. doi: 10.1186/s40623-018-0862-0

Nosé, M., Matsuoka, A., Kumamoto, A., Kasahara, Y., Goldstein, J., Teramoto, M., ... MacDowall, R. J. (2018). Longitudinal structure of oxygen torus in the inner magnetosphere: Simultaneous observations by Arase and Van Allen Probe A. *Geophysical Research Letters*, *45*(19), 10,177–10,184. doi: 10.1029/2018GL080122

Nosé, M., Oimatsu, S., Keika, K., Kletzing, C. A., Kurth, W. S., Pascuale, S. D., ... Larsen, B. A. (2015). Formation of the oxygen torus in the inner magnetosphere: Van Allen Probes observations. *Journal of Geophysical Research: Space Physics*, *120*(2), 1182–1196. doi: 10.1002/2014JA020593

Ober, D. M., Horwitz, J. L., & Gallagher, D. L. (1997). Formation of density troughs embedded in the outer plasmasphere by subauroral ion drift events. *Journal of Geophysical Research: Space Physics*, *102*(A7), 14595–14602. doi: 10.1029/97JA01046

Pavlov, A. V., & Buonsanto, M. J. (1997). Comparison of model electron densities and temperatures with Millstone Hill observations during undisturbed periods and the geomagnetic storms of 16âĂŞ23 March and 6âĂŞ12 April 1990. *Annales Geophysicae*, *15*(3), 327–344. doi: 10.1007/s00585-997-0327-4

Pierrard, V., & Lemaire, J. F. (2004). Development of shoulders and plumes in the frame of the interchange instability mechanism for plasmapause formation. *Geophysical Research Letters*, *31*(5). doi: 10.1029/2003GL018919

Reeves, G. D. (2007). Radiation belt storm probes: A new mission for space weather forecasting. *Space Weather*, *5*(11). doi: 10.1029/2007SW000341

Reinisch, B. W., Moldwin, M. B., Denton, R. E., Gallagher, D. L., Matsui, H., Pierrard, V., & Tu, J. (2009). Augmented empirical models of plasmaspheric density and electric field using IMAGE and CLUSTER data. *Space Sci. Rev.*, *145*, 1231–1261. doi: 10.1007/s11214-008-9481-6

Roberts, W. T., Horwitz, J. L., Comfort, R. H., Chappell, C. R., Waite Jr., J. H., & Green, J. L. (1987). Heavy ion density enhancements in the outer plasmasphere. *Journal of Geophysical Research: Space Physics*, *92*(A12), 13499–13512. doi: 10.1029/JA092iA12p13499

Roelof, E. C. (1987). Energetic neutral atom image of a storm-time ring current. *Geophysical Research Letters*, *14*(6), 652–655. doi: 10.1029/GL014i006p00652

Stern, D. P. (1975). The motion of a proton in the equatorial magnetosphere. *Journal of Geophysical Research*, *80*(4), 595–599. doi: 10.1029/JA080i004p00595

Takahashi, K., Ohtani, S.-i., Denton, R. E., Hughes, W. J., & Anderson, R. R. (2008). Ion composition in the plasma trough and plasma plume derived from a Combined Release and Radiation Effects Satellite magnetoseismic study. *Journal of Geophysical Research: Space Physics*, *113*(A12). doi: 10.1029/2008JA013248

Volland, H. (1973). A semiempirical model of large-scale magnetospheric electric fields. *Journal of Geophysical Research*, *78*(1), 171–180. doi: 10.1029/JA078i001p00171

Weimer, D. R. (2005). Improved ionospheric electrodynamic models and applications to calculating Joule heating rates. *Journal of Geophysical Research*, *110*. doi: 10.1029/2004JA010884